Perovskite solar cells with CuSCN hole extraction layers yield stabilized efficiencies >20%

Neha Arora,[1‡] M. Ibrahim Dar,[1‡*] Alexander Hinderhofer,[2] Norman Pellet,[1] Frank Schreiber,[2] Shaik Mohammed Zakeeruddin,[1] Michael Grätzel[1*]

Affiliations:

[1] Laboratory of Photonics and Interfaces, Department of Chemistry and Chemical Engineering, Swiss Federal Institute of Technology Lausanne, Lausanne CH-1015, Switzerland.

[2] Institut für Angewandte Physik, Universität Tübingen, 72076 Tübingen, Germany

*Correspondence authors: (M.I.D.) E-mail: ibrahim.dar@epfl.ch, (M.G.) E-mail: michael.graetzel@epfl.ch

‡ These authors have contributed equally to the work

Abstract: Perovskite solar cells (PSC) with efficiencies > 20% have only been realized with highly expensive archetype organic hole transporting materials that can impede the large-scale deployment of PSC. Here we demonstrate PSCs achieving stabilized efficiencies of 20.3% with CuSCN as hole electron extraction layer. We developed a new method for the solution deposition of compact and highly conformal CuSCN layers that afford fast carrier extraction and collection. We also show that the notorious instability of CuSCN based PSCs is not associated with the CuSCN/perovskite interface but rather originates from the CuSCN/Au contact. By introducing a thin spacer layer between CuSCN and gold layers, the PSCs retained >95% of their initial efficiency after aging for 500 h under full-sun illumination at 60 °C, and >85% of their initial efficiency after aging at 85 °C for 1000 h. Importantly, under both continuous illumination and thermal stress, CuSCN based devices surpass the stability of spiro-OMeTAD based PSCs.

One Sentence Summary: A record performance displayed by operationally stable perovskite solar cells employing all-inorganic charge extraction layers was realized after introducing a simple dynamic approach for the deposition of thin and conformal CuSCN layer onto perovskite layer and a thin spacer layer between CuSCN and gold layers, which will foster their large scale deployment.

The prominence of organic-inorganic perovskite solar cells (PSC) can be credited to the unprecedented advancement in the power conversion efficiencies (PCEs), realized mostly by tailoring the formation and composition of the absorber layer (*1,2*). Certified PCEs >20% have been obtained while retaining the electron selective TiO_2 layer and by using either spiro-OMeTAD [2,2′,7,7′-tetrakis(*N*,*N*-di-p-methoxyphenyl-amine)9,9′-spirobifluorene] or a polymer-based PTTA (*poly*-triarylamine) as the hole-transporting material (HTM) (*2,3*). However, the cost of these HTMs is prohibitively high for large-scale applications and the long-term operational and thermal instability seems to be associated with the archetype organic HTMs or their ingredients (*4*). One of the strategies to combat the issues of cost and instability could be the use of inexpensive inorganic hole extraction layers similar to the use of TiO_2 as an electron transporting material (*5*). However, obtaining stable PCEs >20% with PSCs using inorganic

HTMs, such as NiO, CuI, Cs_2SnI_6, and CuSCN when subjected to light soaking under realistic operational conditions, i.e., at maximum power point and 60°C has remained a challenge (*6-9*).

The realization of efficiencies > 20% using PSCs with inorganic HTMs remains undoubtedly a key goal to foster the large-scale deployment of PSC. Among various inorganic hole transporting materials, CuSCN is an extremely cheap, abundant *p*-type semiconductor, that exhibits high hole mobility, a good thermal stability and a well-aligned work function (*10*). The CuSCN is intrinsically *p*-doped and transmits light across the entire visible and near infrared spectral region, so it is also attractive for tandem cell applications where the PSC is placed on top of a lower band gap semiconductor (*11*). However, the stabilized PCE values reported with CuSCN lag far behind devices based on the standard spiro-OMeTAD. For CuSCN deposition, different methods, including doctor blading, electrodeposition, spin coating, and spray coating have been tried (*9, 12-15*). Of those, the solution-based bottom-up approaches are more facile; however, a critical issue associated with them is that most of the solvents in which CuSCN shows high solubility degrade the perovskite layer (*16*). Primarily, because the dearth of solvents that readily dissolve CuSCN but not the perovskites, an inverted device architecture has been employed albeit with moderate success (*12*).

In order to retain the mesoscopic TiO_2-based normal device architecture, we develop here a simple dynamic deposition method. Typically, we deposited a thin and uniform CuSCN layer on top of $CsFAMAPbI_{3-x}Br_x$ ($MA=CH_3NH_3^+$, $FA= CH(NH_2)_2^+$) perovskite layer without compromising on the latter's quality by drop-casting a defined volume of CuSCN dissolved in diethyl sulfide in 2 to 3 s while spinning the substrate at 5000 rpm. The structural features of the resulting CuSCN layer were investigated using x-ray diffraction (XRD). CuSCN crystallizes in two polymorphs, α-CuSCN (*17*) and β-CuSCN (*18,19*), where the latter exhibits polytypism, i.e., a variation in layer stacking order. A comparison of the calculated powder XRD spectra and grazing-incidence x-ray diffraction (GIXD) data of CuSCN (**Fig. 1A**) shows the dynamic deposition method yielded β-CuSCN. A broad reflection at $q=1.9$ $Å^{-1}$ established the presence of different polytypes of β-CuSCN, predominantly 2H and 3R. Coherently scattering island sizes of 17 and 18 nm were estimated using the peak width of the (002) reflection of CuSCN deposited, respectively, on the glass and perovskite film. Furthermore, to determine the domain orientation, we acquired grazing-incidence wide-angle x-ray scattering (GIWAXS) data from CuSCN and CuSCN/perovskite films (**Fig. 1, B and C**). From the intensity distribution of the (002) β-CuSCN ring (**fig. S1**), it is evident that the CuSCN domains have preferential orientation with the long unit cell axis parallel to the substrate (**Fig. 1, D and E**).

Scanning electron microscopy (SEM) micrographs of the perovskite film acquired before (**Fig. 2A**) and after (**Fig. 2B**) the deposition of CuSCN layer revealed the homogeneous coverage of the perovskite overlayer with the CuSCN layer. By comparison, for a spiro-OMeTAD layer deposited via the conventional spin coating method, the presence of pinholes is quite evident (**fig. S2a**), which could be detrimental to performance (*20*). To evaluate the thickness of various layers, we acquired the cross-sectional SEM micrograph (**Fig. 2C**) of the complete device, which established the formation of ~60-nm thin CuSCN layer sandwiched between a perovskite overlayer and a gold layer. Diethyl sulphide is a highly polar solvent, which can arguably damage the underneath perovskite layer. Therefore, to minimize the interaction between perovskite and diethyl sulphide solvent, we applied dynamic deposition approach in which the solvent evaporated rapidly as compared to conventional deposition approach thus minimizing the interaction between perovskite and diethyl sulphide. In addition, the rapid evaporation of solvent

induces nucleation and growth of CuSCN nanostructures. In fact, high density of nucleation leads to the formation of compact and thin CuSCN film composed of nano-crystallites.

We investigated the charge-carrier dynamics in pristine and HTM-containing perovskite films using steady-state photoluminescence (PL) and time-correlated single photon counting (TCSPC) spectroscopy. The pristine perovskite film exhibited an intense PL emission centered around 773 nm with a linewidth of 44 nm (**Fig. 2D**). In the presence of a charge-extraction layer, the PL of the pristine perovskite film was strongly quenched, from which very rapid extraction of electrons or holes across the interfaces could be inferred (*21*). We used TCSPC spectroscopy to estimate the dynamics of charge carriers quantitatively (**Fig. 2E**). The long lifetime of the charge carriers (τ_{10} = 390 ns) is indicative of the high electronic quality of the pristine perovskite film. (τ_{10} is the time at which the initial PL intensity decreases by a factor of 10) (*22*). In agreement with the steady-state PL, the charge-carrier lifetime decreased sharply in the perovskite films containing TiO_2 (τ_{10} = 49 ns) as electron extraction layer, and spiro-OMeTAD (τ_{10} = 22 ns) or CuSCN (τ_{10} = 16 ns) as hole extraction layer. In comparison, the hole injection from the valence band of perovskite into the highest occupied molecular orbital (HOMO) of HTM was more rapid than the electron injection from the conduction band of perovskite into that of TiO_2 (*23*). In addition, TCSPC showed that the hole transfer was faster across the perovskite-CuSCN junction as compared to the perovskite-spiro-OMeTAD interface, although the thermodynamic driving force (difference between the two energy levels) is lower at the perovskite-CuSCN interface (*24*). This difference could be explained by considering that there are stronger interfacial interactions between the Pb ions of the perovskite and sulfide of CuSCN than with the organic layer.

Apart from injection, transport of charges through the HTM layer is another critical process that strongly influences the overall device performance. In fully assembled solar cells, hole mobilities of 1.4×10^{-6} cm^2 v^{-1} s^{-1} and 1.2×10^{-3} cm^2 v^{-1} s^{-1} were assessed for spiro-OMeTAD and CuSCN, respectively, by using the photo-charge extraction and linearly increasing voltage (*25*). With similar charge separation and recombination dynamics in the perovskite, the ~ 1000 times higher hole mobility and thinner layer of CuSCN presents a distinct advantage over spiro-OMeTAD enabling the former HTM to be effective in its pristine form in contrast to the latter, which requires a high concentration of *p*-dopant and other additives, such as organic lithium salt and 4-*tert*-butylpyridine to reach its peak performance.

After the successful deposition of the thin and conformal β-CuSCN layer, we investigated the photovoltaic (PV) characteristics of the devices. The PV parameters extracted from the current-voltage (*J-V)* curve **(Fig. 3A)** of spiro-OMeTAD based device yielded a short-circuit current J_{SC} of 23.35 mA cm^{-2}, an open-circuit voltage V_{OC} of 1137 mV, and a fill factor *FF* of 77.5 % resulting in an overall efficiency of 20.8%. The device with CuSCN as HTM yielded a J_{SC} of 23.40 mA cm^{-2}, V_{OC} of 1103 mV, and a *FF* of 77.2% resulting in a PCE of 20.3% **(Fig. 3B)**. As evident from the hysteresis index values, hysteresis effect was discernable for spiro-OMeTAD by comparing the forward and backward *J-V* scan, but it was negligible for CuSCN (**Fig. 3C**) (*26*). **Fig. 3C** shows that the V_{OC} yielded by CuSCN based devices was slightly lower compared to spiro-OMeTAD based ones. To understand the cause of the V_{OC} deficit in CuSCN containing devices, we estimated the ideality factor (*n*), which is an indicator of the dominant recombination mechanism occurring within a working device (*27*).

By fitting the intensity dependence of the V_{OC} curves (**Fig. 3A, B; insets**) using the equation S1, *n* of 1.46 and 1.51 were estimated, respectively, for the spiro-OMeTAD and CuSCN based devices, which indicates that the difference in the V_{OC} stemmed from marginally higher

monomolecular recombination occurring within the CuSCN-based devices. Fig. 3C summarizes the statistical analysis of PV parameters extracted from the *J-V* curves of 20 independent devices. The high PCEs were not merely reproducible for spiro-OMeTAD based PSCs but also for CuSCN ones, as we observed an average J_{SC} = 22.77 ± 0.49 mA cm^{-2}, V_{OC} = 1090 ± 11 mV, and *FF* = 0.74 ± 0.02 resulting in an average PCE of 19.34 ± 0.75% for CuSCN-based devices. Similarly, for the spiro-OMeTAD based devices, an average PCE of 19.6 ± 0.77%, with an average J_{SC} = 22.6 ± 0.55 mA cm^{-2}, V_{OC} = 1115 ± 15 mV, and *FF* = 0.75± 0.02 was recorded. Furthermore, to determine the stabilized (scan-speed independent) PCEs, the solar cells were probed at their maximum power point under full-sun illumination (**Fig. 3D**). We recorded a stabilized output power corresponding to a PCE of 20.5% and 20.3% for spiro-OMeTAD and CuSCN based devices, respectively, in close agreement with the *J-V* measurements. The integrated photo-current densities obtained from the external quantum efficiency (EQE) spectra of spiro-OMeTAD- and CuSCN-based devices agreed closely with those obtained from the *J-V* curves (**Fig. 3E**), indicating that any spectral mismatch between our simulator and AM-1.5 standard solar radiation was negligible.

The manifestation of the long-term operational stability is a crucial requirement for future exploitations of PSCs based technology (*28*). Under full-sun illumination at a maximum power point, the CuSCN devices showed extremely poor photo-stability losing over 50% of their initial efficiency merely within 24 h (**Fig. 3F, red trace**). In the literature, such an instability of PSCs has been associated with the degradation of CuSCN/perovskite interface (*14*), however, deposition of ~2 nm Al_2O_3 layer between perovskite and CuSCN layer using ALD showed insignificant effect on the initial degradation (**fig. S3**). In an unprecedented move, we introduced a thin rGO spacer layer between CuSCN and gold layers, which astoundingly led to the realization of excellent operational stability under full-sun illumination at 60 °C as the resulting PSCs retained over 95% of their initial efficiency after aging for 500 h, apparently surpassing the stability of *spiro*-OMeTAD devices recorded under similar conditions (**fig. S4**). Further insight about the degradation was gained through X-ray photoelectron spectroscopy, which establishes the oxidation of gold (**fig. S6**) when CuSCN devices are subjected to the light soaking test. Therefore, we contend that the instability of PSCs is not associated with the degradation of CuSCN/perovskite interface as is generally believed but rather originates majorly from the CuSCN/Au contact. Furthermore, demonstrating the long-term thermal stability at high temperature has become imperative, primarily, because the diffusion of metal through spiro-OMeTAD layer at higher temperatures leads to the degradation of the devices (*20*). We examined the thermal stability of CuSCN-based devices coated with a thin layer of polymer at 85°C in ambient conditions in the dark. After 1000 h, the CuSCN-based devices retained >85% of their initial efficiency (**fig. S7**). The formation of uniform CuSCN film, as evident from morphological analysis, blocked the metal diffusion (*20*). Importantly, the CuSCN film did not require any additives to function as effective HTM in contrast to PTAA and *spiro*-OMeTAD, which can reach their peak performance only in the presence of LiTFSI and 4-*tert*-butylpyridine and, for the latter, also a Co(III) complex that acts as *p*-dopant. These additives readily cross into the photoactive PSC layer and adversely affect PV performance (**fig. S7**). The comparative analysis of stability tests shows that the severe degradation observed under operational conditions is driven by light, and this effect is worth to investigate further. Such a record PCE together with a remarkable operational stability and thermal stability displayed by the PSC employing all-inorganic charge extraction layers, i.e., mesoporous TiO_2 and CuSCN, will foster their large scale deployment.

References and Notes:

1. A. Kojima, K. Teshima, Y. Shirai, T. Miyasaka, Organometal Halide Perovskites as Visible-Light Sensitizers for Photovoltaic Cells. *J. Am. Chem. Soc.* **131**, 6050-6051 (2009).
2. W. S. Yang *et al.*, High-performance photovoltaic perovskite layers fabricated through intramolecular exchange. *Science* **348**, 1234 (2015).
3. Bi *et al.*, Polymer-templated nucleation and crystal growth of perovskite films for solar cells with efficiency greater than 21%. *Nature Energy* **1**, 16142 (2016).
4. J. Liu et al., A dopant-free hole-transporting material for efficient and stable perovskite solar cells. *Energy Environ. Sci.* **7**, 2963-2967 (2014).
5. H.-S. Kim *et al.*, Lead Iodide Perovskite Sensitized All-Solid-State Submicron Thin Film Mesoscopic Solar Cell with Efficiency Exceeding 9%. *Sci. Rep.* **2**, 591 (2012).
6. W. Chen *et al.*, Efficient and stable large-area perovskite solar cells with inorganic charge extraction layers. *Science* **350**, 944 (2015).
7. J. A. Christians, R. C. M. Fung, P. V. Kamat, An Inorganic Hole Conductor for Organo-Lead Halide Perovskite Solar Cells. Improved Hole Conductivity with Copper Iodide. *J. Am. Chem. Soc.* **136**, 758-764 (2014).
8. I. Chung, B. Lee, J. He, R. P. H. Chang, M. G. Kanatzidis, All-solid-state dye-sensitized solar cells with high efficiency. *Nature* **485**, 486-489 (2012).
9. P. Qin *et al.*, Inorganic hole conductor-based lead halide perovskite solar cells with 12.4% conversion efficiency. *Nature Communications* **5,** 3834 (2014).
10. J. E. Jaffe *et al.*, Electronic and Defect Structures of CuSCN. *J. Phys. Chem. C* **114**, 9111-9117 (2010).
11. J. W. Jung, C.-C. Chueh, A. K. Y. Jen, High-Performance Semitransparent Perovskite Solar Cells with 10% Power Conversion Efficiency and 25% Average Visible Transmittance Based on Transparent CuSCN as the Hole-Transporting Material. *Adv. Energy Mater.* **5**, 1500486 (2015).
12. S. Ye *et al.*, CuSCN-Based Inverted Planar Perovskite Solar Cell with an Average PCE of 15.6%. *Nano Lett.* **15**, 3723-3728 (2015).
13. M. Jung *et al.*, Thermal Stability of CuSCN Hole Conductor-Based Perovskite Solar Cells. *ChemSusChem* **9**, 2592-2596 (2016).
14. Liu, J. *et al.* Identification and Mitigation of a Critical Interfacial Instability in Perovskite Solar Cells Employing Copper Thiocyanate Hole-Transporter. *Advanced Materials Interfaces* **3**, 1600571 (2016).
15. S. Ye *et al.*, A strategy to simplify the preparation process of perovskite solar cells by co-deposition of a hole-conductor and a perovskite layer. *Adv. Mater.* **28**, 9648-9654 (2016).
16. N. Yaacobi- Gross *et al.*, High- efficiency organic photovoltaic cells based on the solution-processable hole transporting interlayer copper thiocyanate (CuSCN) as a replacement for PEDOT:PSS. *Adv. Energy Mater.* **5**, 1401529 (2015).

17. M. Kabešová, M. Dunaj-jurčo, M. Serator, J. Gažo, J. Garaj, The crystal structure of copper(I) thiocyanate and its relation to the crystal structure of copper(II) diammine dithiocyanate complex. *Inorganica Chimica Acta* **17**, 161-165 (1976).
18. D. L. Smith, V. I. Saunders, The structure and polytypism of the [beta] modification of copper(I) thiocyanate. *Acta Crystallographica Section* B **37**, 1807-1812 (1981).
19. D. L. Smith, V. I. Saunders, Preparation and structure refinement of the 2H polytype of β-copper(I) thiocyanate. *Acta Crystallographica Section B* **38**, 907-909 (1982).
20. Y. Han et al., Degradation observations of encapsulated planar $CH_3NH_3PbI_3$ perovskite solar cells at high temperatures and humidity. *J Mater. Chem. A* **3**, 8139-8147 (2015).
21. S. D. Stranks *et al.*, Electron-hole diffusion lengths exceeding 1 micrometer in an organometal trihalide perovskite absorber. *Science* **342**, 341 (2013).
22. L. Kong et al., Simultaneous band-gap narrowing and carrier-lifetime prolongation of organic–inorganic trihalide perovskites. *PNAS* **113**, 8910-8915 (2016).
23. G. Xing *et al.*, Long-range balanced electron- and hole-transport lengths in organic-inorganic $CH_3NH_3PbI_3$. *Science* **342**, 344 (2013).
24. Pydzińska et al., Determination of interfacial charge-transfer rate constants in perovskite solar cells. *ChemSusChem* **9**, 1647-1659 (2016).
25. W. H. Nguyen, C. D. Bailie, E. L. Unger, M. D. McGehee, Enhancing the hole-conductivity of spiro-OMeTAD without oxygen or lithium salts by using spiro$(TFSi)_2$ in perovskite and dye-sensitized solar cells. *J. Am. Chem. Soc.* **136**, 10996-11001 (2014).
26. H.-S. Kim, N.-G. Park, Parameters affecting I–V hysteresis of $CH_3NH_3PbI_3$ perovskite solar cells: effects of perovskite crystal size and mesoporous TiO_2 layer. *J. Phys. Chem. Lett.* **5**, 2927-2934 (2014).
27. K. Tvingstedt *et al.*, Radiative efficiency of lead iodide based perovskite solar cells. *Sci. Rep*. **4**, 6071 (2014).
28. F. Bella et al., Improving efficiency and stability of perovskite solar cells with photocurable fluoropolymers. *Science* 354, 203 (2016).
29. M. Saliba et al., Cesium-containing triple cation perovskite solar cells: improved stability, reproducibility and high efficiency. *Energy Environ. Sci.* **9**, 1989-1997 (2016).
30. C. F. Macrae *et al.*, Mercury: visualization and analysis of crystal structures. *J. Appl. Cryst.* **39**, 453-457 (2006).

Acknowledgments: N.A., M.I.D. and M.G. conceived the idea of the work. N.A and M.I.D. designed the project, fabricated and characterized devices. M.I.D. and N.A. performed photoluminescence and SEM analysis. N.A, M.I.D. and A.H. performed the XRD measurements. A.H. and F.S. analyzed and discussed the XRD data. N.P. carried out hole mobility and light soaking measurements. M.I.D. wrote the manuscript, and all the authors contributed towards finalizing the draft. S.M.Z. coordinated the project. M.G. directed and supervised the research. N. A. gratefully acknowledge financial support from Dyesol. M. I. D., S. M. Z. and M. G. thank the King Abdulaziz City for Science and Technology (KACST) and thank funding from the European Union's Horizon 2020 programme, through a FET Open research and innovation action under grant agreement No. 687008. We acknowledge the European Synchrotron Radiation Facility (ESRF) for provision of synchrotron radiation and we would like to thank Andrei Chumakov and Federico Zontone for assistance in using beamline ID10. We thank Jan Hagenlocher for his assistance with XRD analysis, Dr. M. Mayer for his assistance with ALD, and Dr. F. Giordano and Dr. P. Yadav for the helpful discussion. All results are presented in the main paper and supplement.

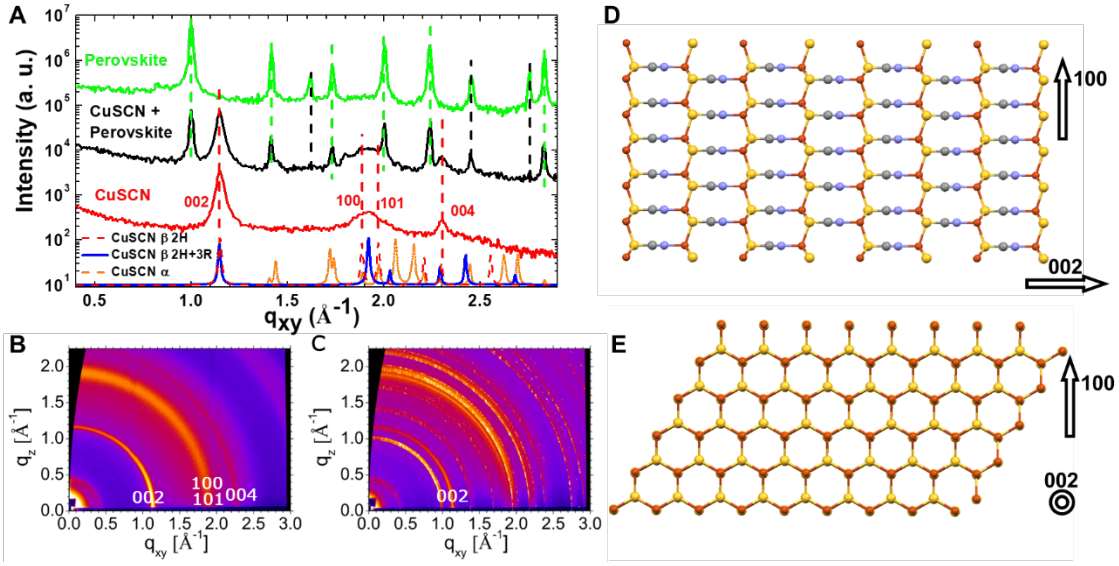

Fig. 1. Structural characterization of pristine and CuSCN coated perovskite films. (A) GIXD data acquired from pure CuSCN on glass, CuSCN on perovskite/TiO_2/FTO and bare perovskite/ TiO_2/FTO. At the bottom, calculated powder diffraction data from CuSCN is shown for comparison. Indexing of CuSCN pattern is performed according to the CuSCN 2H β-structure (black vertical lines correspond to the substrate). (B) GIWAXS data from CuSCN (C) GIWAXS data from CuSCN+perovskite. In image (C) the (002) reflection is clearly visible. Other reflections are super-imposed with more intense reflections from perovskite film. (D) and (E) Images depict the preferential out-of-plane orientation, (the in-plane orientation is rotated by 90°); the red balls represent copper atoms, the yellow balls represent sulfur atoms, the grey balls represent carbon atoms, and the blue balls represent nitrogen atoms.

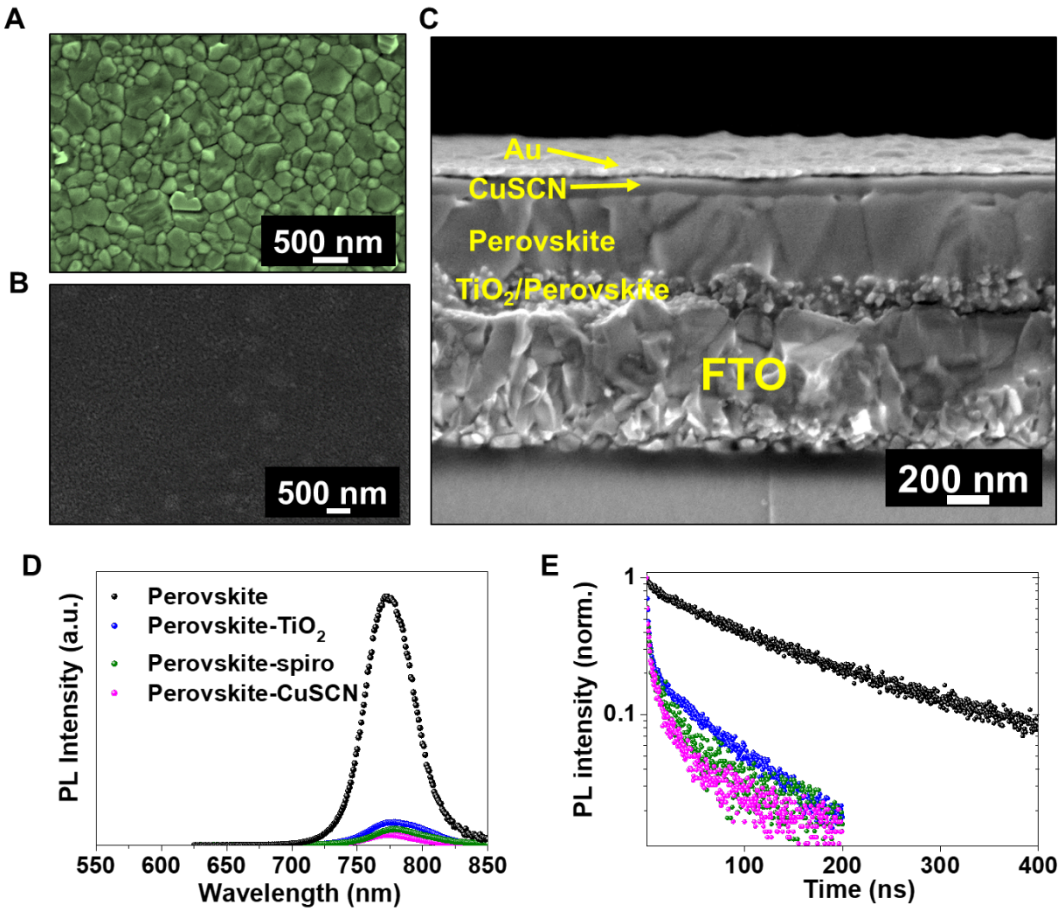

Fig. 2. Morphological characterization of pristine and CuSCN coated perovskite samples and steady-state and time-resolved photoluminescence studies performed on the pristine and perovskite films containing different charge extraction layers. (A) Top-view SEM micrograph of the perovskite film deposited onto mesoporous TiO_2 showing the presence of perovskite grains. (B) Top-view SEM micrograph showing the formation of uniform CuSCN layer deposited onto perovskite film. (C) Cross- sectional SEM micrograph displaying the thickness of different layers of the complete device. (D) Steady-state PL spectra showing strong quenching of intense PL exhibited by the pristine perovskite film. (E) TCSPC showing long lasting charge carriers in pristine perovskite film and the very rapid injection of charges from the perovskite film into the electron and hole extraction layers. (The color code for Fig. 2D and E is the same).

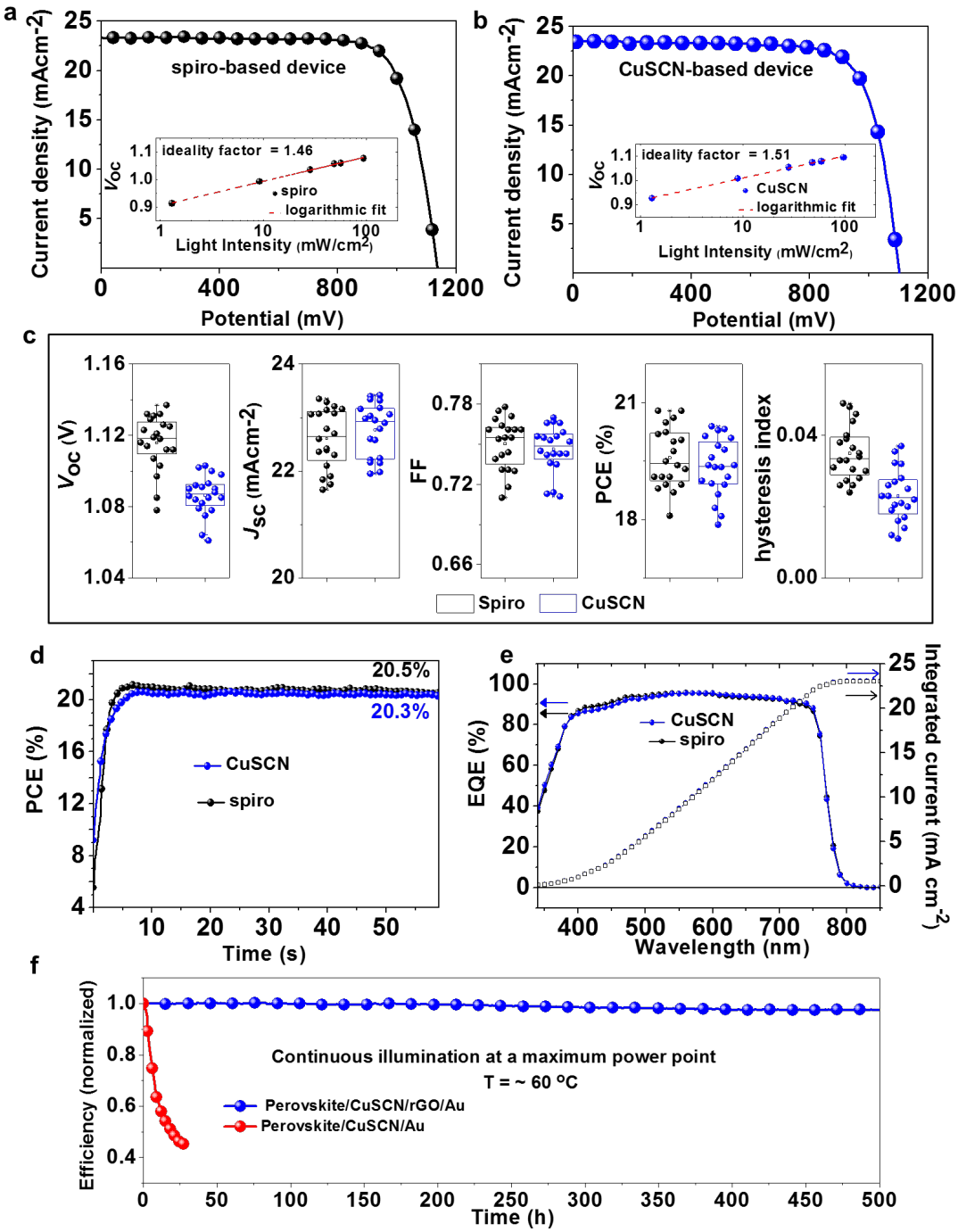

Fig. 3. Photovoltaic characterization of devices based on spiro-OMeTAD and CuSCN hole transporting layers. (A) *J-V* curve of the spiro-OMeTAD based device recorded at a scan rate of 0.01 V s^{-1}; the inset shows the V_{OC} as a function of illumination intensity with an ideality factor of 1.46. (B) *J-V* curve of the CuSCN based device recorded at a scan rate of 0.01 V s^{-1}; the inset shows the V_{OC} as a function of illumination intensity with an ideality factor of 1.51. (C) *J-V* metrics for 20 independent devices based on spiro-OMeTAD and CuSCN. (D) The maximum power point (MPP) tracking for 60 s yielding a stabilized efficiency of 20.5 and 20.3%, respectively, for spiro-OMeTAD and CuSCN based devices. (E) EQE as a function of

monochromatic wavelength recorded for spiro-OMeTAD and CuSCN based devices and the integrated current densities obtained from the respective EQE spectra. (F) Operational stability of un-encapsulated CuSCN based device (PCE = 20.03%, fig. S5) containing a thin layer of rGO (as a spacer layer between perovskite and gold layers), examined at a maximum-power-point under continuous full-sun illumination at 60 °C in nitrogen atmosphere.

Supplementary Materials:

Materials and Methods

Supplementary Text

Figures S1-S11

Tables S1

References

Supplementary Materials for

Perovskite solar cells with CuSCN hole extraction layers yield stabilized efficiencies >20%

Neha Arora,[1‡] M. Ibrahim Dar,[1‡*] Alexander Hinderhofer,[2] Norman Pellet,[1] Frank Schreiber,[2] Shaik Mohammed Zakeeruddin,[1] Michael Grätzel[1*]

*Correspondence authors: (M.I.D.) E-mail: ibrahim.dar@epfl.ch, (M.G.) E-mail: michael.graetzel@epfl.ch

This PDF file includes:

Materials and Methods

All materials were purchased from Sigma-Aldrich and were used as received unless stated otherwise.

Preparation of TiO_2 photoanode

Fluorine-doped tin oxide (FTO)-glass substrates (TCO glass, NSG 10, Nippon sheet glass, Japan) were cleaned by ultrasonication in Hellmanex (2%, deionized water) for 30 min, rinsed thoroughly with de-ionized water and ethanol, and then treated in oxygen plasma for 15 min. A compact layer of TiO_2 of ca 30 nm was subsequently deposited via spray pyrolysis at 450 °C from a precursor solution of commercial titanium diisopropoxide bis(acetylacetonate) (75% in 2-propanol, Sigma-Aldrich) diluted in anhydrous ethanol (1:9, volume ratio) and oxygen as a carrier gas. A mesoporous TiO_2 layer was then deposited by spin coating a diluted paste at a spin speed of 4000 rpm, acceleration 2000 rpm for 20 s (the weight ratio of TiO_2 (Dyesol paste, 30NRD) and ethanol is 1:6), onto the substrate containing TiO_2 compact layer. This was followed by sintering the substrates at 450 °C for 30 min in dry air flow. For Li treatment of the mesoporous TiO_2 scaffold, 150 µL of LiTFSI (bis(trifluoromethylsulfonyl)imide lithium salt) solution in acetonitrile (10mg/mL, freshly prepared in argon atmosphere) was spin coated (3000 rpm, acceleration 2000 rpm for 20 s) after a loading time of 10 s. Thereafter, Li-treated substrates were subjected to a second sintering step at 450 °C for 30 min in dry air. The substrates were transferred in a dry air glove box (humidity< 1%) after cooling down to 200 °C for perovskite deposition.

Preparation of perovskite

The perovskite films were deposited using single-step deposition method from the precursor solution containing FAI (1.0 M) (Dyesol), PbI_2 (1.1 M) (TCI), MABr (0.2 M) (Dyesol) and $PbBr_2$ (0.2 M) (TCI) in anhydrous dimethylformamide (99.8%, Acros) / dimethylsulphoxide (99.7%, Acros) (4:1 (v:v)). Thereafter, CsI (abcr, GmbH, ultra dry; 99.998%), (5% volume, 1.5 M DMSO) was added to the precursor solution (*29)*. The precursor solution was spin-coated onto the mesoporous TiO_2 films in a two-step programme at 1000 and 6000 r.p.m. for 10 and 30 s, respectively. During the second step, 100 µl of chlorobenzene (99.8%, Acros) was dropped on the spinning substrate 10 s prior to the end of the programme. This was followed by annealing the films at 100 °C for 45 min. The perovskite deposition was carried out in a dry air glove box under controlled atmospheric conditions with humidity <1%.

Deposition of hole transporting layer

To complete the fabrication of devices, 2,2',7,7'-tetrakis(*N*,*N*-di-*p*-methoxyphenylamine)-9,9-spirobifluorene (spiro-OMeTAD, 70 mM in chlorobenzene) as a hole-transporting material (HTM) was deposited by spin coating 40 µL of the prepared solution at 4000 rpm for 30 s. The spiro-OMeTAD (Merck) was doped with bis(trifluoromethylsulfonyl)imide lithium salt, tris(2-(1H-pyrazol-1-yl)-4-tert-butylpyridine)- cobalt(III) tris(bis(trifluoromethylsulfonyl) imide) (FK 209, from

Dyenamo) and 4-tert-Butylpyridine (96%, Sigma-Aldrich) in a molar ratio of 0.5, 0.03 and 3.3, respectively.

CuSCN solution was prepared by dissolving CuSCN salt (99%, Sigma-Aldrich) in 1 mL of diethyl sulfide (98%, Sigma-Aldrich) after constant stirring at room temperature for 30 min. To deposit a thin and uniform film of CuSCN, 35 µL of a CuSCN solution were drop casted within 2-3 seconds on the substrate containing perovskite film spinning at 5000 rpm, and the substrate was allowed to spin for 30 seconds. Like in case of spiro-OMeTAD deposition, no post heat treatment was applied. The deposition of hole transporting layer was carried out in a dry air glove box with humidity <1%. Finally, device fabrication was completed by thermally evaporating ~60 nm of gold layer as a back contact.

Deposition of Al_2O_3 spacer layer.

Al_2O_3 was deposited from trimethylaluminium ($Al(CH_3)_3$) (Sigma Aldrich) and deionized H_2O using Savannah ALD system from Cambridge Nanotech, USA. The precursors were pulsed into the reactor using N_2 (99.999%) as an inert carrier gas. The water was pulsed for 0.015 s and confined in the reactor for 60 s followed by purging of TMA for 0.015 s, and wait another 60 s. 20 ALD cycles were applied to achieve the thickness of ~2 nm.

Deposition of rGO spacer layer.

A thin layer (~10 nm thickness) of reduced graphene oxide (Ossila (flake size 0.1-1 µm, flake thickness <1nm, purity>99%)) was deposited by spin coating the solution (filtered) containing reduced graphene oxide (1 mg/mL in chlorobenzene, sonicated for 30 min) at 3000 rpm onto the CuSCN layer.

Structural characterization

X-ray scattering experiments were done at beamline ID10 EH1 of the ESRF with a photon energy of 22 keV under nitrogen atmosphere. The beam size was 10 µm in vertical direction and 120 µm in horizontal direction. GIXD data was measured under an angle of incidence of 0.08° with a point detector. GIWAXS data was measured with a PILATUS 300k area detector under the same angle of incidence. Calculation of powder diffraction data was done with mercury (*30*).

Morphological characterization

A field-emission scanning electron microscope (Merlin) was used to examine the morphology of the perovskite films and the thickness of various layers. An electron beam accelerated to 3 kV was used with an in-lens detector.

Charge extraction by linearly increasing voltage

Fully assembled devices were connected to a function generator and measured with an oscilloscope across a small load resistance to minimize the RC effects of the circuit. The mobilities were measured across a range of electric fields, which are determined by the field at the time where the maximum current is extracted.

Photoluminescence studies

Photoluminescence and time-resolved photoluminescence spectra were recorded on a spectrofluorometer Fluorolog 322. Photoluminescence spectra were recorded by exciting the samples with 450 W Xenon lamp at a fixed wavelength of 450 nm and scanning the emission monochromator from 625 to 850 nm. The same spectrometer

working in a time-correlated single-photon counting mode was used for the measurements of photoluminescence decay kinetics with sub-nanosecond time resolution. Picosecond pulsed diode laser head NanoLED-405LH (Horiba) emitting <200 ps duration pulses at 408 nm with repetition rate of 1 MHz was used as an excitation source. For electron injection study, the samples were excited from the TiO_2 side while as to study the photoluminescence decay kinetics in pristine and HTM containing samples, the samples were excited from the top.

Photovoltaic studies

The current-voltage (J-V) characteristics of the perovskite devices were recorded with a digital source meter (Keithley model 2400, USA). A 450 W xenon lamp (Oriel, USA) was used as the light source for photovoltaic (*J-V*) measurements. The light source was equipped with a Schott K113 Tempax sunlight filter (Praezisions Glas and Optik GmbH) to match the emission spectrum of the lamp to the AM1.5G standard. Before each measurement, the exact light intensity was determined using a calibrated Si reference diode equipped with an infrared cutoff filter (KG-3, Schott) The photo-active area of 0.16 cm^2 was defined using a dark-colored metal mask. External quantum efficiency (EQE) measurements were made using a LED light source (Ariadne EQE from Cicci Research).

Stability Test

Photo-stability tests were carried out at a maximum power point under one-sun illumination at 60 °C using a home-built electronic board with an eight-channel maximum power point capability. The channels were equipped with DACs (DAC7563), level shifters (INA2132), and an output line driver (OPA2192). The driving line had a 12 bit resolution in the ±2.048 V range (1 mV per bit). The buffer output was connected to the cells through a 0.5 Ohm sense resistor. The voltage drop was amplified (INA188) to sense the current. The voltage was buffered (OPA2188) to sense the voltage. The signal lines were multiplexed (CD54HC4051) into a fourth order active Butterworth filter with its pole set at 500 Hz. Data conversion was performed at 430 SPS by an analog to digital converter (ADS1118). The DACs and the ADC were interfaced by an Atmega328 microcontroller. The light source consisted of an array of white LEDs was powered by a constant current and no filters (UV) were used. Equivalent sun intensities were calibrated using a calibrated Si reference diode equipped with a KG-3 filter. The setup was calibrated periodically using a Keithley 2602B source-measuring unit. For thermal stability tests, CuSCN based devices were coated with a thin layer (30 nm) of PMMA (20mg/mL in chlorobenzene) atop the gold layer. Thermal stability tests were performed by ageing the devices at 85 °C in an oven and the photovoltaic efficiency under AM1.5 simulated sun light was periodically recorded.

Supplementary Text

The intensity dependence of V_{OC} curves (**Fig. 3A, B; insets**) were fitted using the following equation:

Equation S1: $V_{OC} = \frac{nkT}{q} \ln\left(\frac{Jsc}{J_0}\right)$

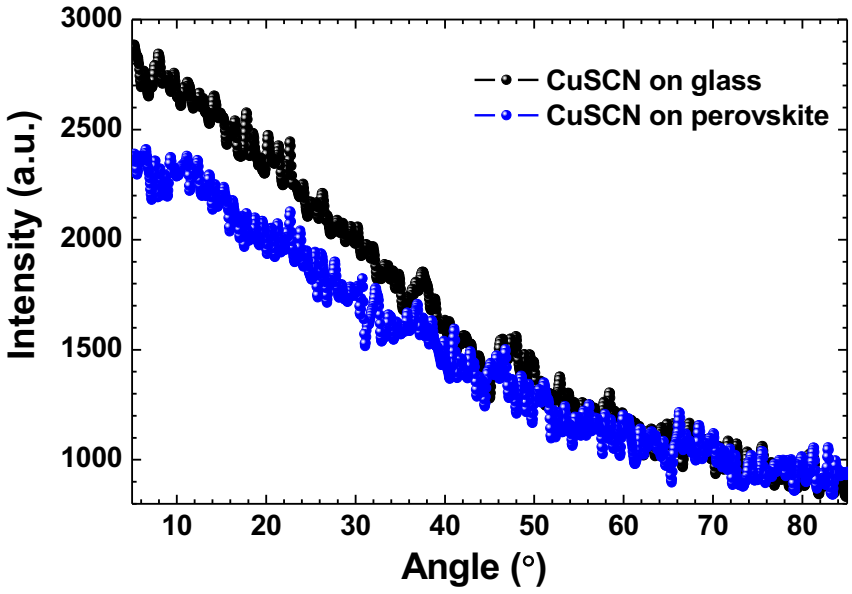

Fig. S1. Intensity distribution of β-CuSCN. Angular distribution of intensity from the CuSCN (002) reflection on glass and perovskite after background subtraction. (0° is parallel to the substrate plane; 90° is perpendicular).

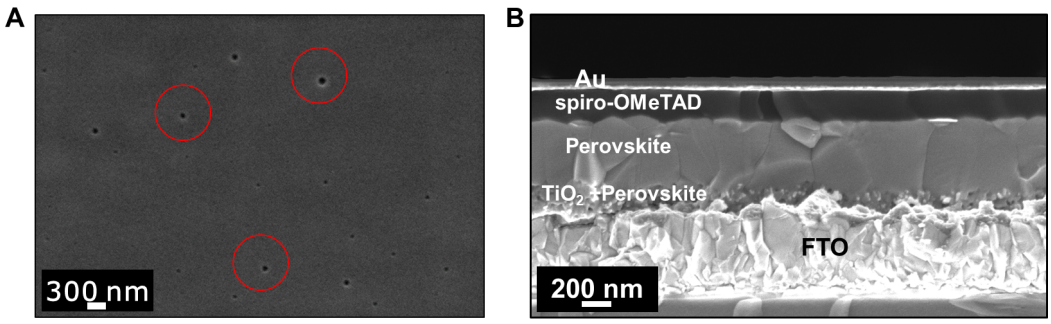

Fig. S2. Morphological characterization of spiro-OMeTAD coated perovskite film and spiro-OMeTAD based PSC. (A) Top-view SEM micrograph of spiro-OMeTAD layer deposited onto perovskite film showing the presence of pin holes. (B) Cross section SEM micrograph displaying the thickness of different layers of the complete device.

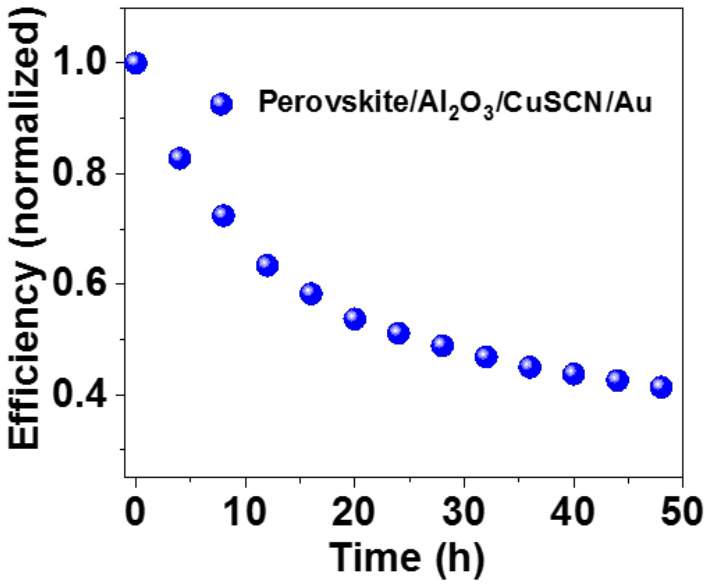

Fig. S3. Operational stability of CuSCN based devices with Al_2O_3 (20 cycles). Photo-stability examined at a maximum-power-point under continuous full-sun illumination at 60 °C in nitrogen atmosphere.

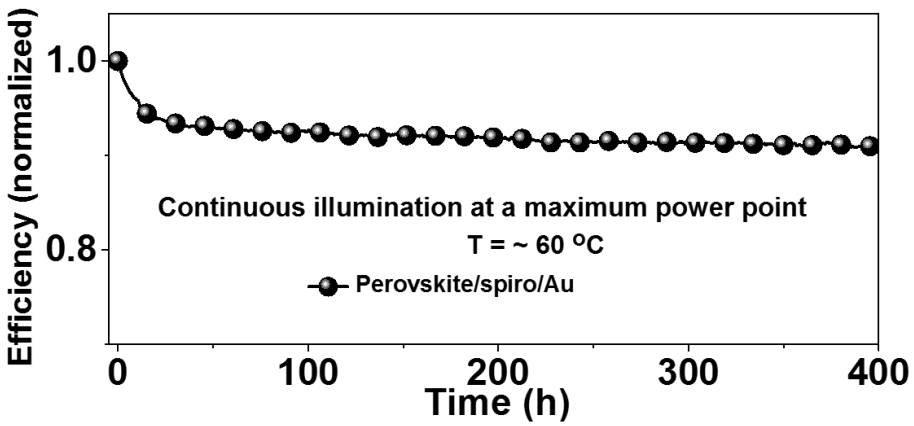

Fig. S4. Operational stability of un-encapsulated spiro-OMeTAD based device. Photo-stability examined at a maximum-power-point under continuous full-sun illumination at 60 °C in nitrogen atmosphere.

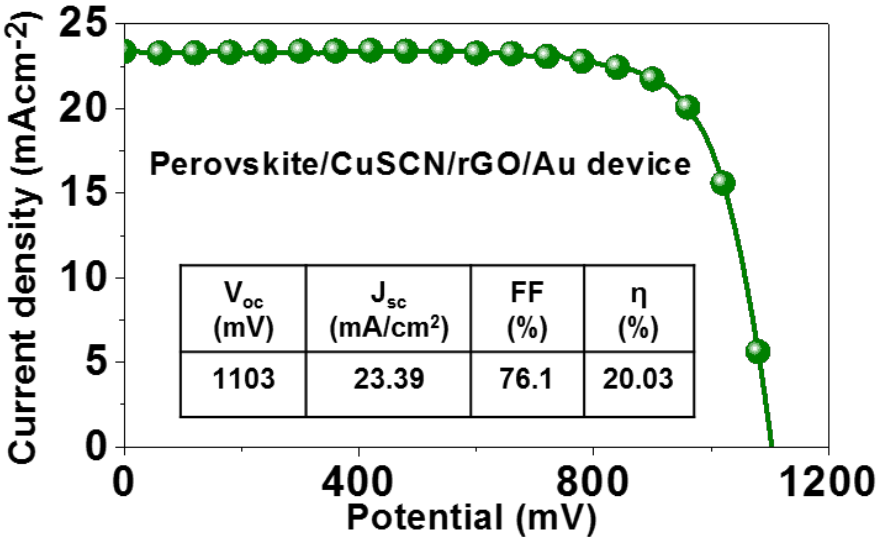

Fig. S5. Photovoltaic characterization. J-V characteristic of the best CuSCN device containing a thin layer of rGO as a spacer layer between perovskite and gold layers recorded at a scan rate of 10 mV/s (reverse scan).

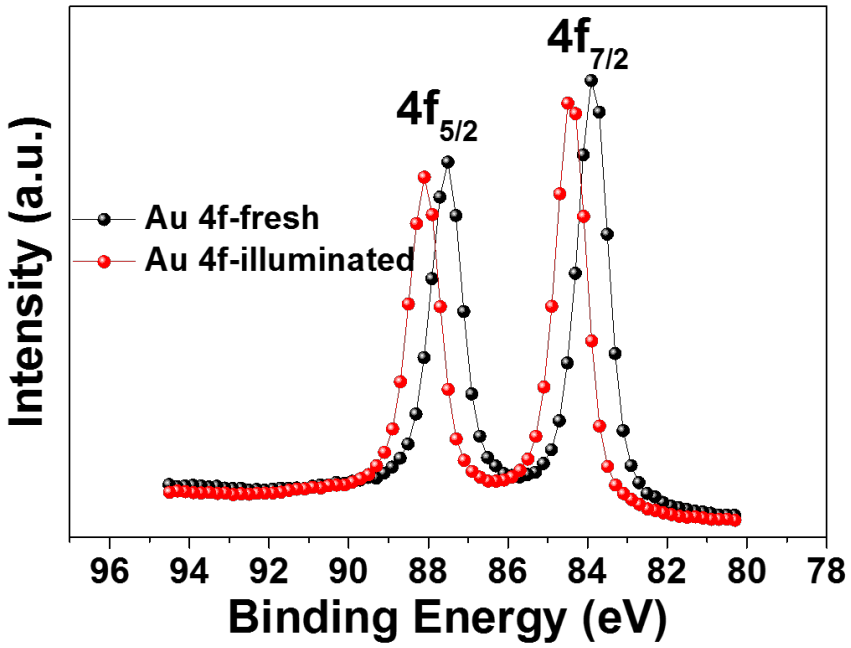

Fig. S6. X-ray photoelectron spectroscopy. Core shell Au 4f spectra recorded from freshly deposited gold layer and the gold layer removed from CuSCN based device illuminated at a maximum-power-point at 60 °C for 50 h.

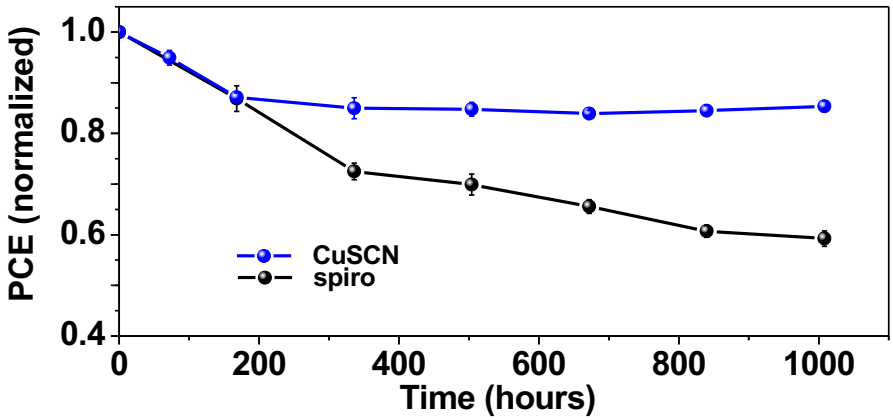

Fig. S7. Stability test at 85 °C. Thermal stability test of spiro-OMeTAD (sealed device) and CuSCN (coated with a thin layer of PMMA) based perovskite solar cells aged at 85 °C in air for 1000 h in the dark. The error bars represent the standard deviation of a batch of four solar cells.

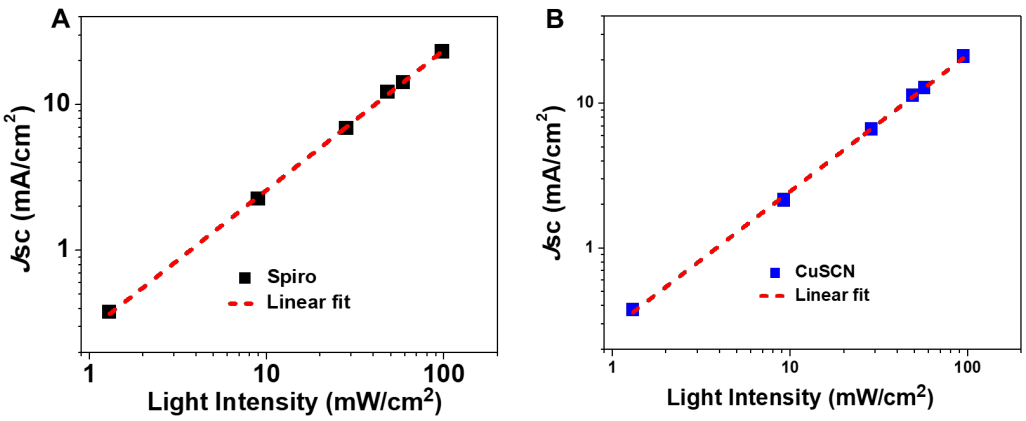

Fig. S8. The J_{SC} (log scale) as a function of illumination intensity. (A) Light intensity dependence of J_{SC} in spiro-OMeTAD based device (Black solid squares) red color solid line: linear fit. **(B)** Light intensity dependence of J_{SC} in CuSCN based device (Blue solid squares) red color solid line: linear fit.

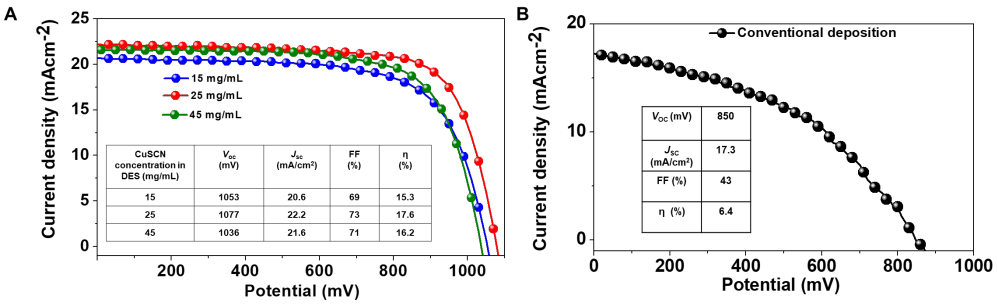

CuSCN concentration in DES (mg/mL)	V_{oc} (mV)	J_{sc} (mA/cm²)	FF (%)	η (%)
15	1053	20.6	69	15.3
25	1077	22.2	73	17.6
45	1036	21.6	71	16.2

Fig. S9. Photovoltaic characterization. (A) J-V characteristics of the best devices obtained after employing concentration of 15, 25, and 45 mg/mL of CuSCN in diethyl sulfide recorded at a scan rate of 0.05 V/s (reverse scans). (Inset shows the photovoltaic parameters extracted from the JV curves). **(B)** J-V curves of the best CuSCN based device involving conventional deposition of CuSCN recorded at a scan rate of 0.05V/s. (Inset shows the photovoltaic parameters extracted from the JV curve).

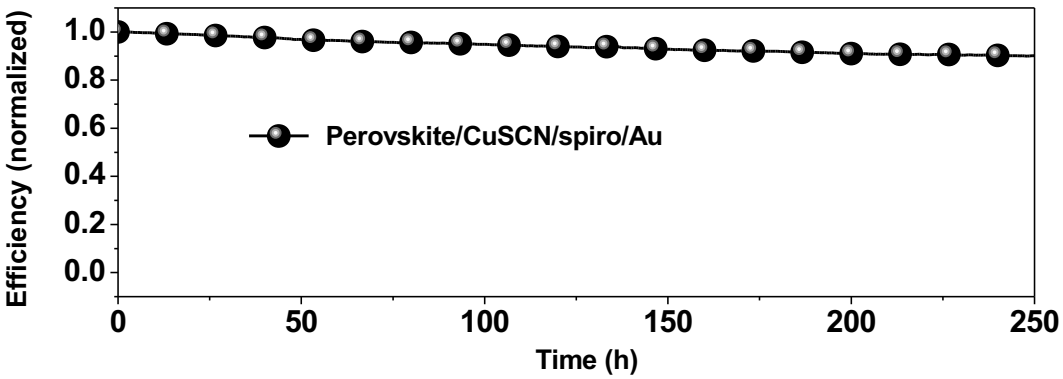

Fig. S10. Operational stability of un-encapsulated CuSCN based device containing a thin layer of spiro (as a spacer layer between perovskite and gold layers), examined at a maximum-power-point under continuous full-sun illumination at 60 °C in nitrogen atmosphere.

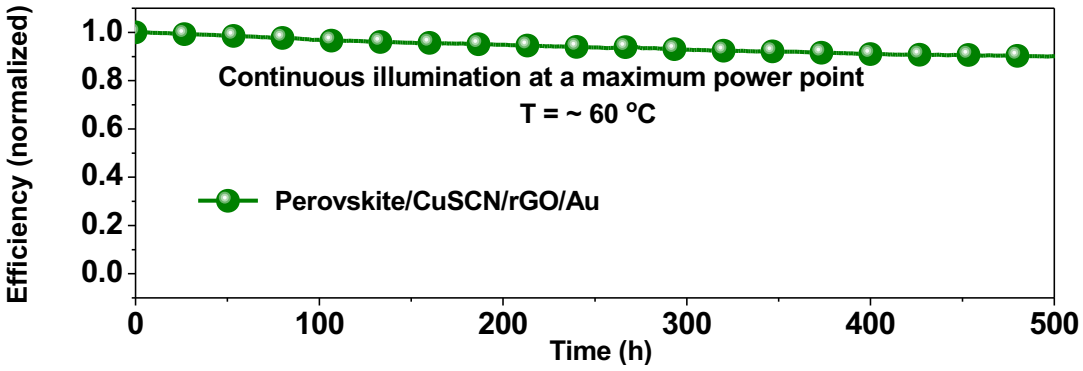

Fig. S11. Operational stability of un-encapsulated CuSCN based device (second device) containing a thin layer of rGO (as a spacer layer between perovskite and gold layers), examined at a maximum-power-point under continuous full-sun illumination at 60 °C in nitrogen atmosphere.

Table S1. Photovoltaic parameters extracted from the JV curves (Figure 3A, B) of the best performing spiro-OMeTAD and CuSCN based devices measured at reverse and forward scans.

	Scan direction	**V_{oc} (mV)**	**J_{sc} (mA/cm^2)**	**FF (%)**	**η (%)**
spiro	Backward	1137	23.35	77.5	20.8
	Forward	1129	23.31	75.5	20.1
CuSCN	Backward	1103	23.40	77.2	20.3
	Forward	1097	23.41	76.3	20.0

References and Notes:

References and Notes:

1. A. Kojima, K. Teshima, Y. Shirai, T. Miyasaka, Organometal Halide Perovskites as Visible-Light Sensitizers for Photovoltaic Cells. *J. Am. Chem. Soc.* **131**, 6050-6051 (2009).
2. W. S. Yang *et al.*, High-performance photovoltaic perovskite layers fabricated through intramolecular exchange. *Science* **348**, 1234 (2015).
3. Bi *et al.*, Polymer-templated nucleation and crystal growth of perovskite films for solar cells with efficiency greater than 21%. *Nature Energy* **1**, 16142 (2016).
4. J. Liu et al.,. A dopant-free hole-transporting material for efficient and stable perovskite solar cells. *Energy Environ. Sci.* **7**, 2963-2967 (2014).
5. H.-S. Kim *et al.*, Lead Iodide Perovskite Sensitized All-Solid-State Submicron Thin Film Mesoscopic Solar Cell with Efficiency Exceeding 9%. *Sci. Rep.* **2**, 591 (2012).
6. W. Chen *et al.*, Efficient and stable large-area perovskite solar cells with inorganic charge extraction layers. *Science* **350**, 944 (2015).
7. J. A. Christians, R. C. M. Fung, P. V. Kamat, An Inorganic Hole Conductor for Organo-Lead Halide Perovskite Solar Cells. Improved Hole Conductivity with Copper Iodide. *J. Am. Chem. Soc.* **136**, 758-764 (2014).
8. I. Chung, B. Lee, J. He, R. P. H. Chang, M. G. Kanatzidis, All-solid-state dye-sensitized solar cells with high efficiency. *Nature* **485**, 486-489 (2012).
9. P. Qin *et al.*, Inorganic hole conductor-based lead halide perovskite solar cells with 12.4% conversion efficiency. *Nature Communications* **5,** 3834 (2014).
10. J. E. Jaffe *et al.*, Electronic and Defect Structures of CuSCN. *J. Phys. Chem. C* **114**, 9111-9117 (2010).
11. J. W. Jung, C.-C. Chueh, A. K. Y. Jen, High-Performance Semitransparent Perovskite Solar Cells with 10% Power Conversion Efficiency and 25% Average Visible Transmittance Based on Transparent CuSCN as the Hole-Transporting Material. *Adv. Energy Mater.* **5**, 1500486 (2015).
12. S. Ye *et al.*, CuSCN-Based Inverted Planar Perovskite Solar Cell with an Average PCE of 15.6%. *Nano Lett.* **15**, 3723-3728 (2015).
13. M. Jung *et al.*, Thermal Stability of CuSCN Hole Conductor-Based Perovskite Solar Cells. *ChemSusChem* **9**, 2592-2596 (2016).
14. Liu, J. *et al.* Identification and Mitigation of a Critical Interfacial Instability in Perovskite Solar Cells Employing Copper Thiocyanate Hole-Transporter. *Advanced Materials Interfaces* **3**, 1600571 (2016).
15. S. Ye *et al.*, A strategy to simplify the preparation process of perovskite solar cells by co-deposition of a hole-conductor and a perovskite layer. *Adv. Mater.* **28**, 9648-9654 (2016).

16. N. Yaacobi- Gross *et al.*, High- efficiency organic photovoltaic cells based on the solution- processable hole transporting interlayer copper thiocyanate (CuSCN) as a replacement for PEDOT:PSS. *Adv. Energy Mater.* **5**, 1401529 (2015).

17. M. Kabešová, M. Dunaj-jurčo, M. Serator, J. Gažo, J. Garaj, The crystal structure of copper(I) thiocyanate and its relation to the crystal structure of copper(II) diammine dithiocyanate complex. *Inorganica Chimica Acta* **17**, 161-165 (1976).

18. D. L. Smith, V. I. Saunders, The structure and polytypism of the [beta] modification of copper(I) thiocyanate. *Acta Crystallographica Section* B **37**, 1807-1812 (1981).

19. D. L. Smith, V. I. Saunders, Preparation and structure refinement of the 2H polytype of β-copper(I) thiocyanate. *Acta Crystallographica Section B* **38**, 907-909 (1982).

20. Y. Han et al., Degradation observations of encapsulated planar $CH_3NH_3PbI_3$ perovskite solar cells at high temperatures and humidity. *J Mater. Chem. A* **3**, 8139-8147 (2015).

21. S. D. Stranks *et al.*, Electron-hole diffusion lengths exceeding 1 micrometer in an organometal trihalide perovskite absorber. *Science* **342**, 341 (2013).

22. L. Kong et al., Simultaneous band-gap narrowing and carrier-lifetime prolongation of organic–inorganic trihalide perovskites. *PNAS* **113**, 8910-8915 (2016).

23. G. Xing *et al.*, Long-range balanced electron- and hole-transport lengths in organic-inorganic $CH_3NH_3PbI_3$. *Science* **342**, 344 (2013).

24. Pydzińska et al., Determination of interfacial charge-transfer rate constants in perovskite solar cells. *ChemSusChem* **9**, 1647-1659 (2016).

25. W. H. Nguyen, C. D. Bailie, E. L. Unger, M. D. McGehee, Enhancing the hole-conductivity of spiro-OMeTAD without oxygen or lithium salts by using spiro$(TFSi)_2$ in perovskite and dye-sensitized solar cells. *J. Am. Chem. Soc.* **136**, 10996-11001 (2014).

26. H.-S. Kim, N.-G. Park, Parameters affecting I–V hysteresis of $CH_3NH_3PbI_3$ perovskite solar cells: effects of perovskite crystal size and mesoporous TiO_2 layer. *J. Phys. Chem. Lett.* **5**, 2927-2934 (2014).

27. K. Tvingstedt *et al.*, Radiative efficiency of lead iodide based perovskite solar cells. *Sci. Rep*. **4**, 6071 (2014).

28. **F. Bella et al.,** Improving efficiency and stability of perovskite solar cells with photocurable fluoropolymers. *Science* 354, 203 (2016).

29. M. Saliba et al., Cesium-containing triple cation perovskite solar cells: improved stability, reproducibility and high efficiency. *Energy Environ. Sci.* **9**, 1989-1997 (2016).

30. C. F. Macrae *et al.*, Mercury: visualization and analysis of crystal structures. *J. Appl. Cryst.* **39**, 453-457 (2006).